Thermal fluid dynamics of the effect of filler wire on deposition rate and bead formation intending plasma arc-based DED

Xin Chen [a,*], Chong Wang [a,*], Jialuo Ding [a], Rongdong Qu [a], Yipeng Wang [a,b], Goncalo Pardal [a], Stewart Williams [a]

[a] *Welding and Additive Manufacturing Centre, Cranfield University, Cranfield MK43 0AL, UK*
[b] *School of Materials Science and Engineering, Beijing University of Technology, Beijing, China*

ARTICLE INFO

ABSTRACT

The influence of filler wire configuration, such as size and geometry, on the deposition rate (DR) and bead formation, has been studied in wire arc-based directed energy deposition (WADED), but the fundamental physics underlying its effect on wire melting and melt pool dynamics remains unclear. In this paper, a series of plasma arc-based DED (plasma-DED) experiments were conducted to investigate the impact of five different filler wire configurations on DR and bead dimensions. The coupling behaviours of wire melting, metal transfer and melt pool dynamics under the five filler wire configurations were also simulated numerically using the authors' recently developed wire-feeding model. The calculated wire melting and bead cross-sections are consistent with the experimental images and measurements. The results demonstrate that the filler wire significantly affects the highest DR by altering wire melting and metal transfer behaviours through changes in arc energy absorption. The filler wire with a rhombus geometry which is closer to a Gaussian-like arc distribution than the flat wire was shown to get higher DR and more stable metal transfer. Furthermore, different filler wire configurations lead to distinct melt pool behaviours, including temperature distribution and flow velocity, due to various metal transfer behaviours and arc shading effects. This study sheds light on the fundamental physics underlying the impact of filler wire on wire melting and bead formation for the first time. The methods and findings can guide improving DR and controlling bead shape in the plasma-DED process.

1. Introduction

Additive manufacturing (AM) is a game-changing technology that can be used with a wide range of materials, including metallic ones, for structure applications [1–5]. AM constructs three-dimensional (3D) parts layer-by-layer based on digital models, eliminating the need for expensive molds or tools typically required by conventional manufacturing methods [4]. Among metallic AM methods, wire arc-based directed energy deposition (WADED) stands out as the very suitable for medium and large-scale component manufacturing, thanks to its cost-effectiveness and high productivity [5,6]. This technique holds enormous potential in various industries, including aerospace, defence, energy, and transportation [5–9]. However, it remains crucial to develop a comprehensive understanding of the fundamental physics of this rapidly evolving technique and its application.

In the WADED process, an arc plasma melts a filler wire, which transfers to the substrate or previous layer and solidifies to create a deposit. Compared to tungsten inert gas (TIG) and metal inert gas (MIG) arcs, a plasma arc is a stable higher-energy-density heat source [10,11] that delivers high-accuracy beads and products [10]. The filler wire configuration, including its size and geometry, could significantly affect the process quality and deposition rate (DR) in plasma arc-based DED (plasma-DED), where a round filler wire with 0.6–1.2 mm diameter is commonly used. Increasing wire feeding speed (WFS) changes the DR, and the wire melting and metal transfer behaviour, leading to a shift in metal transfer mode from globular to droplet-liquid bridge to solid-liquid bridge, and altering process stability [12]. The globular mode causes instability that could result in humping and undercut defects, and the solid-liquid bridge mode has low process tolerance and may cause violent disturbances in the melt pool [10]. Therefore, to ensure a stable deposition process, it is crucial to maintain the droplet-liquid bridge mode.

In the plasma DED process, achieving higher DRs with constant process parameters can be possible by adjusting the filler wire

---

arrangement or plasma gas mixture. Preheating a wire or using a hot wire can improve wire melting and DR, but it requires additional equipment and energy [13]. Alternatively, using a plasma gas mixture instead of single argon plasma can increase arc energy density and improve wire melting [14,15]. Adjusting the filler wire configuration, such as the size and geometry, is a more straightforward method that does not require extra equipment or gas mixtures. Wang et al. [10] reported that using a thick wire of 2.4 mm increased DR by 25.2 % compared to a thin wire of 1.2 mm, likely due to the thick wire absorbing more arc energy in the lateral direction. Feng et al. [16] observed a significant increase in DR by using dual wires instead of a single wire. Xu et al. [17] used a high DR dual-wire TIG-based DED to manufacture large-scale Ti64 components successfully. Further research is needed to fully understand the effect of filler wire configuration on wire melting and DR.

In addition to DR, the filler wire configuration in the plasma-DED process can impact bead formation by influencing melt pool behaviours. A thick wire can prevent keyhole-induced defects observed in a thin wire, according to Chong et al. [10]. Interactions between the filler wire and arc were found to affect melt pool behaviours and bead formation in both the arc welding and arc-DED processes [12,18–25]. In the plasma-DED process, Ríos et al. [26] demonstrated that the melt pool oscillates due to periodical droplet impingement. Jia et al. [27] developed a constricted plasma-DED method that utilizes small droplets to create a stable melt pool and bead formation. However, the mechanism behind how filler wire configuration influences the melt pool behaviour and bead formation is unclear due to the lack of a reliable method to investigate the impact of filler wire configuration on the heat transfer and fluid flow in the melt pool.

This study aims to investigate the impact of filler wire configuration on the DR and bead formation in plasma-DED, to enhance DR while maintaining good bead formation. To accomplish this, we conducted a set of experiments using five different filler wire configurations and presented the variations of the highest DR. The variations in bead formations while maintaining a constant DR for the same wire material were investigated. Additionally, the wire melting, metal transfer and melt pool dynamics while maintaining a constant DR for the same wire material were numerically simulated using our recently reported wire-feeding model [12]. The calculated wire melting and melt pool dimensions were compared with the experimental images and measurements, demonstrating good agreement. Finally, the study revealed the underlying physics of how the filler wire configuration impacts the DR and bead formation in the plasma-DED process.

2. Materials and methods

2.1. Experimental description

The substrate dimensions used in the experiments were 300 mm × 200 mm × 7 mm for all configurations. Three configurations of round filler wires made from Ti64 alloy, including 1.2 mm, 2.4 mm, and dual 1.2 mm wires, were used as feedstocks and melted and deposited on the Ti64 substrates during the plasma-DED process. The chemical compositions of the Ti64 wires and substrates can be found in Table 1. Originally, the flat titanium wire was also planned to be used in the experiment. However, due to its unavailability, the flat mild steel (MS) [28] wire (rectangle, 5 mm × 0.5 mm) was substituted. To compare with the effect of the flat MS wire, a round MS wire with a 1.2 mm diameter was also used. The chemical compositions of the MS wires and substrates are detailed in Table 2. As a result, the study utilized five distinct filler

Table 1
Chemical composition (in wt%) of the Ti64 wire and substrate.

Al	V	Fe	C	N	H	O	Ti
6.08	3.80	0.122	0.019	0.008	0.001	0.15	Balance

Table 2
Chemical composition (in wt%) of the MS wire and substrate.

C	Si	Mn	Cr	Mo	Fe
0.08	0.6	0.9	2.5	1.0	Balance

wire configurations, and their corresponding names which are referred to in the following sections, have been outlined in Table 3.

A set of plasma-DED experiments were conducted in a glove chamber filled with pure argon gas. The schematic of the experimental setup is shown in Fig. 1. A direct current (DC) torch powered by a plasma power source (EWM T552 Tetrix) was employed. The torch was equipped with a tungsten electrode, having a radius of 1.6 mm and a vertex angle of 45°. The nozzle-to-substrate distance was set at 8.0 mm, with an electrode setback of 1.4 mm. For the plasma and shielding gases, pure argon was used at flow rates of 0.8 and 8 litres per minute (l/min), respectively. The arc current was maintained constantly at 200 A for all experiments.

The arc voltage was measured and recorded using an arc monitor (AMV 4000). The travel speeds were set at 4.5 mm/s for Ti64 wires and 3.0 mm/s for MS wires. As shown in Fig. 2, the wire feeding angles θ were 25° for Ti64 wires and 30° for MS wires. The wire-substrate distances at the arc centerline d_{ws} were 2.4 mm for Ti64 wires and 2.0 mm for MS wires. For the dual Ti wire, the angle between the wires φ was set at 30°. To investigate the wire feeding limits, the wire feeding speed (WFS) was adjusted from 0 to 5 m/min, with intervals ranging from a maximum of 1.0 m/min to a minimum of 0.05 m/min, until the wire made contact with the melt pool. A comprehensive list of the equipment and process parameters used in the experiments is provided in Table 4.

In the plasma-DED experiment, a fundamental bead-on-plate single-layer deposition method was used. The process was recorded using a process camera (Xiris XVC-1000e) at 25 Hz in the longitudinal direction, and an additional camera was used for the dual Ti wire configuration (Fig. 2b) in the lateral direction. The bead surface profiles were captured by the stereoscope, and the bead cross-sections were measured through metallographic analysis and microscopic inspection.

2.2. Numerical simulation

Wire melting, metal transfer, and melt pool dynamics for different filler wire configurations were simulated by using our recently reported wire-feeding model [12]. The geometry model used in simulations is shown in Fig. 3, with a symmetric assumption using the longitudinal slice (plane ABCD) as the plane of symmetry. The movement of the filler wire was described using the mixture theory and the Euler method [29], with the area Θ set as the velocity inlet boundary for wire feeding. The substrate was assumed to move instead of the wire feeder and plasma torch, with a velocity inlet boundary condition applied for plane FILD and a pressure outlet boundary condition for plane EJKC. The symbol definitions are provided in Table 5.

During the plasma-DED, the liquid metal was treated as a laminar, Newtonian, incompressible fluid, and the time-varying liquid-gas interface (free surface) was tracked using the volume of fluid (VOF) method [30]. The VOF method utilizes the volume fraction α to

Table 3
Five filler wire configurations and their corresponding names used in this study.

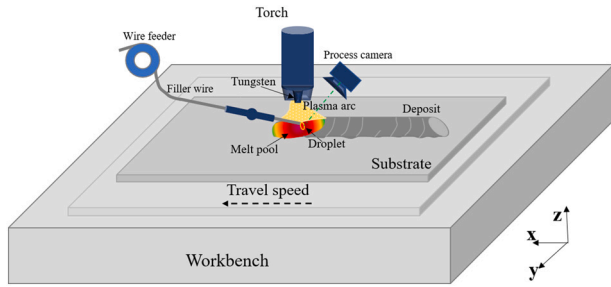| No.	Wire configuration	Materials	Configuration name
1	●, 1.2 mm diameter	Ti64	1.2 mm Ti wire
2	●, 2.4 mm diameter	Ti64	2.4 mm Ti wire
3	●●, 1.2 + 1.2 mm diameter	Ti64	Dual Ti wire
4	●, 1.2 mm diameter	MS (mild steel)	1.2 mm MS wire
5	▬, 5 mm × 0.5 mm	MS (mild steel)	Flat MS wire

Fig. 1. Schematic of the experimental setup.

represent the phases, where $\alpha = 0$ indicates that the cells are full of metal fluid, $\alpha = 1$ indicates that the cells are full of argon gas, and $0 < \alpha < 1$ indicates that the cells are in the transition region. Thus, the dynamic free surface was captured by solving the transport equation of volume fraction [30]:

$$\frac{\partial \alpha}{\partial t} + \nabla \bullet (\alpha \mathbf{u}) = 0 \tag{1}$$

where t and $\mathbf{u}$ are time and velocity vectors, respectively. The normal vector $\boldsymbol{n}$ and the curvature κ of the free surface were obtained by solving the following equations:

$$\boldsymbol{n} = \frac{\nabla \alpha}{|\nabla \alpha|} \tag{2}$$

$$\kappa = -(\nabla \bullet \boldsymbol{n}) \tag{3}$$

The governing equations for incompressible flow are the conservation equations for mass, momentum, and energy. These equations are as follows:

$$\nabla \bullet \mathbf{u} = 0 \tag{4}$$

$$\rho \left(\frac{\partial \mathbf{u}}{\partial t} + \left((\mathbf{u} - \mathbf{u}_t) \bullet \nabla \right) \mathbf{u} \right) = -\nabla p + \nabla \bullet (\mu \nabla \mathbf{u}) + \rho \mathbf{g} - \rho \beta_T \left(T - T_{ref} \right) \mathbf{g} + \mathbf{F}_{em} + \mathbf{F}_s + \mathbf{F}_m. \tag{5}$$

$$\rho \left(\frac{\partial h}{\partial t} + \left((\mathbf{u} - \mathbf{u}_t) \bullet \nabla \right) h \right) = \nabla \bullet (k \nabla T) + q_{heat} + q_{loss} \tag{6}$$

The time-dependent liquid-solid interface (mushy zone) was implicitly tracked by the enthalpy-porosity technique [31] with a liquid fraction β. In this technique, the mushy zone was considered a porous medium, with a linear relationship between the liquid fraction and temperature [32]:

$$\beta = \begin{cases} 0 & T \leq T_s \\ \dfrac{T - T_s}{T_l - T_s} & T_l > T > T_s \\ 1 & T \geq T_l \end{cases} \tag{7}$$

The presence of a mushy zone can significantly impact fluid flow. In this zone, the liquid fraction can act as a blocker, reducing flow and eliminating velocity in the solid region where the liquid fraction is zero. This reduced porosity results in a Darcy force, denoted as $\mathbf{F}_m$, which can be expressed as:

$$\mathbf{F}_m = \frac{(1 - \beta)^2}{\beta^3 + \varepsilon_0} A_{mush} (\mathbf{u} - \mathbf{u}_t - \mathbf{u}_w) \tag{8}$$

where ε_0 was set as 0.001. The A_{mush} was set to 2×10^6, considering a fast velocity drop and convergent computation [33].

The wire-feeding model [12] incorporates a surface heat source model that accounts for the arc shading effects of the filler wire, including the arc energy and pressure shading. Detailed information on the wire-feeding model, boundary conditions, and numerical methods can be found in our previous publication [12].

Five numerical simulations, each corresponding to one of the five wire configurations were performed. In the simulations, we maintained a constant DR for the same wire material: we used the highest DR achieved with the 1.2 mm Ti wire, which was 1.224 kg/h, as a reference for all Ti64 wires. Similarly, for the MS wires, we established a reference using the highest DR of 1.18 kg/h, which was obtained with the 1.2 mm MS wire. The calculation domain range for the half geometry in Fig. 3 was $0 \leq x \leq 38$ mm, $0 \leq y \leq 12$ mm, and $-7 \leq z \leq 6$ mm with a substrate thickness of 7 mm. Non-uniform hexahedral meshes with a minimum size of 0.2 mm were used, and a time step of 2.5×10^{-5}–5×10^{-5}
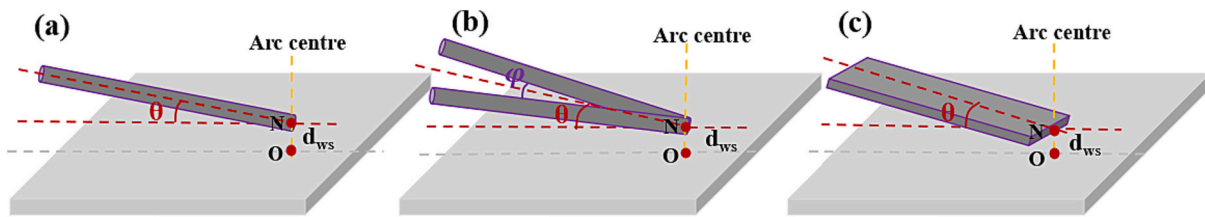

Fig. 2. Schematic of the settings for the five wire configurations: (a) 1.2 mm Ti wire, 2.4 mm Ti wire, 1.2 mm MS wire; (b) dual Ti wire; (c) flat MS wire.

Table 4
Equipment and process parameters used in this study.

| Name	Value (unit)	Name	Value (unit)
Plasma power source	DC EWM T552 Tetrix	Copper nozzle diameter	3.9 mm
Tungsten electrode radius	1.6 mm	Electrode vertex angle	45°
Stand-off distance	8 mm	Electrode setback	1.4 mm
Plasma and shielding gases	Argon	Plasma gas flow rate	0.8 l/min
Shielding gas flow rate	8 l/min	Arc current	200 A
Arc voltage	23.4 V	Travel speed (Ti64)	4.5 mm/s
Travel speed (MS)	3.0 mm/s	wire feeding angle (Ti64)	25°
wire feeding angle (MS)	30°	Wire-substrate distance (Ti64)	2.4 mm
Wire-substrate distance (MS)	2.0 mm	Angle between dual Ti wire	30°
WFS	0–5 m/min	Ambient temperature	27 °C
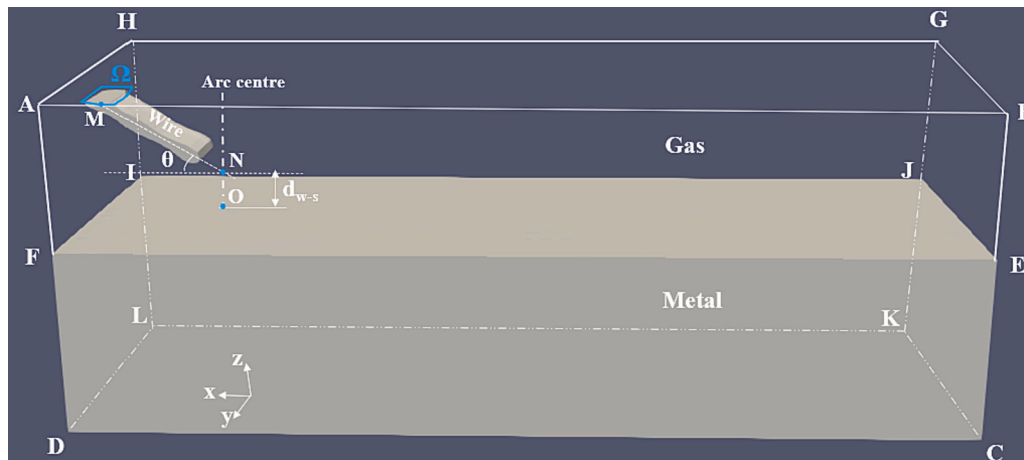
Fig. 3. The geometry model used in the simulations.

Table 5
Nomenclature.

Symbol	Meaning and unit	Symbol	Meaning and unit
A_{mush}	Mushy zone constant, kg m^{-3} s^{-1}	t	Time, s
$\mathbf{F}_{em}$	Momentum source of electromagnetic force, N m^{-3}	$\mathbf{u}$	Velocity vector, m/s
$\mathbf{F}_s$	Momentum sources of surface forces including arc pressure, arc shear stress, surface tension and marangoni shear stress, N m^{-3}	$\mathbf{u}_t$	Velocity vector of travel speed, m/s
$\mathbf{F}_m$	Momentum source of Darcy force, N m^{-3}	$\mathbf{u}_w$	Velocity vector of wire-feeding speed, m/s
$\mathbf{g}$	Acceleration of gravity, m s^{-2}	α	Volume fraction function of fluid
h	Enthalpy, J kg^{-1}	β	Liquid fraction
k	Thermal conductivity, W m^{-1} K^{-1}	β_T	Thermal expansion coefficient, K^{-1}
n	Normal vector to the local free surface, m	κ	Curvature of free surface, m^{-1}
p	Pressure, Pa	ε_0	A small constant avoids the division by zero.
T	Temperature, K	ρ	Density, kg m^{-3}
T_l	Liquidus temperature of Metal, K	σ	Surface tension (ST) coefficient, N m^{-1}
T_s	Solidus temperature of Metal, K	$\dfrac{d\sigma}{dT}$	ST temperature coefficient, N m^{-1} K^{-1}
T_{ref}	Reference temperature, K	μ	Viscosity, Pa s

s was used for convergence. The thermophysical properties of mild steel calculated by the commercial thermophysical software Jmatpro are listed in Table 6, while the properties of Ti64 alloy can be seen in [12].

Table 6
Thermophysical properties of MS and other physical parameters used in the simulations.

Property (unit)	Value
Density (kg m^{-3})	7800
Specific heat (J kg^{-1} K^{-1})	666 (1733 K)
Thermal conductivity (W m^{-1} K^{-1})	30 (1733 K)
Solidus (K)	1693
Liquidus (K)	1733
Latent heat of melting (J kg^{-1})	2.5×10^5
Surface tension coefficient (N m^{-1})	1.7 (1733 K)
Dynamic viscosity (N s m^{-2})	0.006 (1733 K)
Thermal expansion coefficient (K^{-1})	1.5×10^{-5}
Temperature coefficient of surface tension (N m^{-1} K^{-1})	-0.43×10^{-3}
Convective heat transfer coefficient (W m^{-2} K^{-1})	80
Radiation emissivity	0.4

3. Results and discussion

3.1. Experimental results

As shown in Fig. 4a–c, the 1.2 mm Ti wire gradually approached and made contact with the melt pool as the wire feeding speed (WFS) increased from 3.5 m/min to 4.5 m/min. The WFS limit was established based on this contact with the melt pool because, in practice terms, it's not feasible to further increase the wire beyond this point due to the limited tolerance within the process. In comparison to the WFS of 3.5 m/min and 4.5 m/min, the 1.2 mm Ti wire with a WFS of 4.0 m/min was melted and also just made contact with the melt pool. Consequently, the WFS limit for the 1.2 mm Ti wire was determined to be 4.0 m/min.

The deposition rate (DR) is defined as the mass of material deposited per hour and can be expressed using the formula $D_R = \rho u_w S_w$, where ρ represents the wire density, u_w is the WFS and S_w is the cross-sectional area of the wire perpendicular to the feeding direction. The DR reaches its maximum value when the filler wire reaches the WFS limit. By employing this approach, we achieved the highest DRs for the 1.2 mm Ti wire, the 2.4 mm Ti wire and the dual Ti wire at 1.224 kg/h, 1.53 kg/h, and 1.65 kg/h, respectively, as shown in Fig. 4d. These represent increases of 25 % and 34.8 % over the highest DR achieved with the 1.2 mm Ti wire. Furthermore, the highest DR for the 1.2 mm MS wire was 1.18 kg/h, while the highest DR for the flat MS wire reached 2.1 kg/h, representing a substantial increase of 78 %. These results indicate that filler wire configuration significantly affects the maximum DR, potentially through alterations in wire melting and metal transfer behaviours.

In the subsequent sections, we maintained a constant DR for identical wire materials to investigate the effect of wire configuration on wire melting and bead formation. This was achieved by comparing the results across the five wire configurations. For the Ti64 wires, we used the highest DR of 1.224 kg/h, obtained with the 1.2 mm Ti wire, as a reference. Similarly, for the MS wires, we employed the highest DR of 1.18 kg/h, achieved with the 1.2 MS wire, as a reference. The bead formations obtained in experiments for these five wire configurations are presented in Figs. 5 and 6. The results demonstrated a significant variation in bead formation across the five configurations. The bead surface formed using the flat MS wire exhibited large ripples and was not straight (Fig. 5e), while the other configurations produced straight beads with subtle ripples (Fig. 5a–d). As seen in Fig. 6, the bead width using the dual Ti wire was larger than that using the 1.2 mm Ti wire but smaller than that using the 2.4 mm Ti wire. The bead width using the 2.4 mm Ti wire was 13 % larger than that using the 1.2 mm Ti wire. The bead height using the dual Ti wire was larger than that using the 2.4 mm Ti wire but smaller than that using the 1.2 mm Ti wire. The bead height using the 1.2 mm Ti wire was 19 % smaller than that using the 1.2 mm Ti
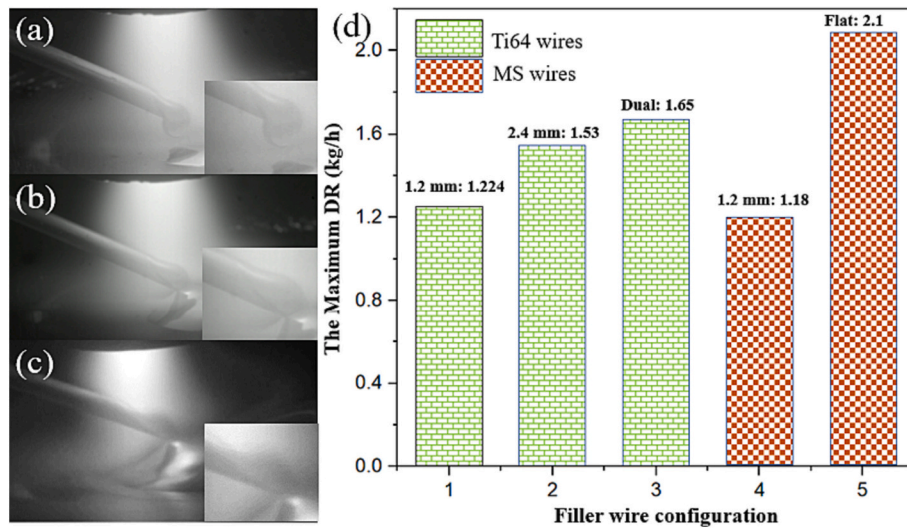
Fig. 4. Wire melting and metal transfer with different WFS for the 1.2 mm Ti wire, and the highest DRs for the configurations 1–5 (d): (a) 3.5 m/min; (b) 4.0 m/min; (c) 4.5 m/min.
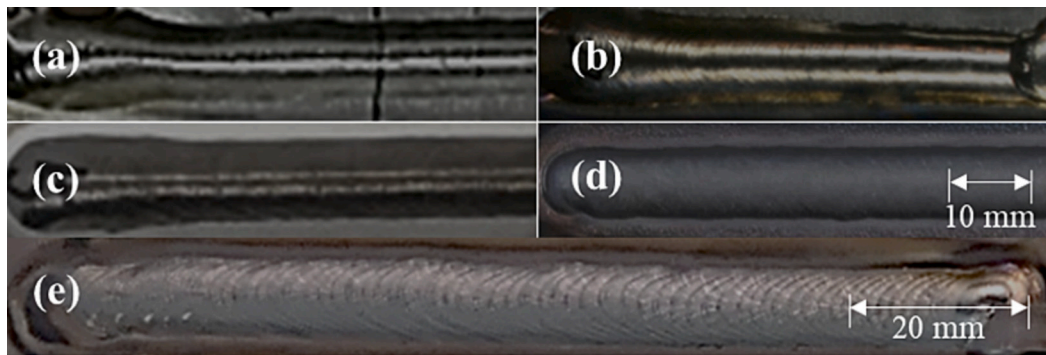

Fig. 5. Bead surfaces for the five wire configurations (the DR for all Ti64 wires is 1.224 kg/h, while 1.18 kg/h for both MS wires): (a) 1.2 mm Ti wire; (b) 2.4 mm Ti wire; (c) dual Ti wire; (d) 1.2 mm MS wire; (e) flat MS wire.
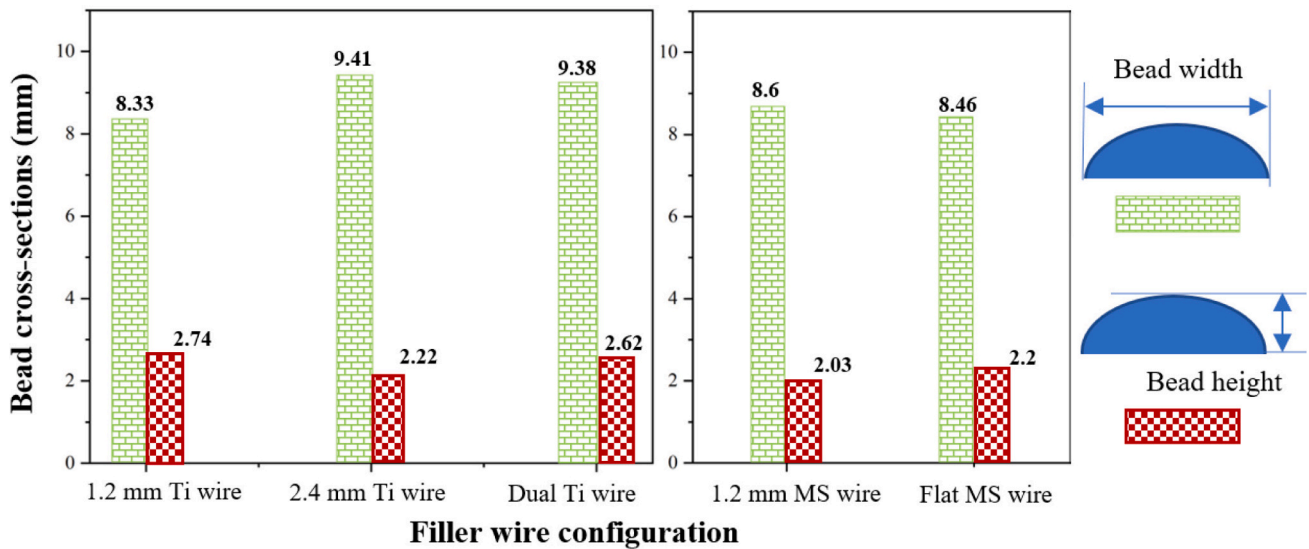

Fig. 6. Bead cross-sections for the five wire configurations (the DR for all Ti64 wires is 1.224 kg/h, while 1.18 kg/h for both MS wires).

wire. Furthermore, the bead width using the flat MS wire was smaller than that using the 1.2 mm MS wire, while the bead height using the flat MS wire was larger than that using the 1.2 mm MS wire. These results imply that the filler wire configuration has a considerable impact on the bead formation, likely through its effects on the heat transfer and fluid flows in the melt pool.

3.2. Simulation validations

The study simulated wire melting and melt pool behaviours using the five filler wire configurations and compared them with experimental results. In the simulations, a constant DR was maintained for identical wire materials: as mentioned above, the DR for all Ti64 wires is 1.224 kg/h, while 1.18 kg/h for both MS wires. Fig. 7 shows the simulated wire melting and its evolution with the dual Ti wire can be seen in Videos 1 and 2 in the attached materials. Fig. 8 illustrates the process images of wire melting and its evolution with the dual Ti wire can be seen in Videos 3 and 4 in the attached materials. The simulation results are consistent with the experimental process images and videos. The melted wire shape and metal transfer position varied significantly depending on the wire configurations. For instance, the melted 1.2 mm Ti wire was connected to the melt pool with a transfer position of 1.2 mm past the arc centre (Fig. 7a), while the melted 2.4 mm Ti wire just touched the melt pool with a transfer position at the arc centre (Fig. 7b). The transfer position of the melted dual Ti wire was close to the arc centre (Fig. 7c). Furthermore, the melted 1.2 mm MS wire was connected with the melt pool with a transfer position of 0.5 mm past the arc centre (Fig. 7e), while the melted flat MS wire with a transfer position of 0.8 mm away from the arc centre (Fig. 7f).

In Fig. 9, the cross-sections of both simulated and experimentally measured beads are presented using the five wire configurations, and the results indicate good agreement between the two sets of data. The bead shape was observed to vary depending on the filler wire configuration used. Table 7 summarizes the comparisons of the bead height, width, and penetration depth between the simulations and experiments, which showed good agreement, with most errors being around or below 10 %. Note that the simulated bead widths in the five cases are all larger than the experimental data. This discrepancy may be attributed to the fact that the model didn't consider the wettability phenomenon [34] during the deposition process. Nonetheless, the comparison of wire melting behaviour (Figs. 7 and 8) and the bead cross-sections (Fig. 9) between the simulations and experiments demonstrated the accuracy of the modelling and simulation in this study.

3.3. Discussion

3.3.1. Wire melting and deposition rate

During the deposition process, the wire was melted completely by the arc when the highest DR was achieved, indicating that the arc's absorption behaviour on the wire, including the absorption area and arc energy distribution, was essential in determining the highest DR. As illustrated in Fig. 10a, the Gaussian-like arc irradiated the filler wire laterally during the plasma-DED process. It was observed that with the same setting and process parameters, the width of the filler wire exposed to the arc significantly influenced the amount of arc energy the wire absorbed in the lateral direction. Consequently, a wider wire led to greater energy absorption and increased melting, which resulted in higher DR. This observation was consistent with the findings in the literature [10]. Furthermore, this study remained a constant of the distance between wire and substrate d_{ws} for the same wire materials. As shown in Fig. 10b, the bottom of the 2.4 mm Ti wire was closer to the substrate than the 1.2 mm Ti wire and more difficult to melt. As a result, the 2.4 mm Ti wire had a shorter furthest wire feeding position and absorbed less arc energy in the longitudinal direction, as it touched the melt pool earlier without fully melting. A higher deposition rate can be obtained for the 2.4 mm Ti wire by using a larger d_{ws}.

Fig. 11 visually depicts the wire melting and furthest wire feeding positions in the longitudinal direction for the five wire configurations. A constant DR was maintained for identical wire materials: as mentioned above, the DR for all Ti64 wires is 1.224 kg/h, while 1.18 kg/h for both MS wires. The furthest wire feeding position with the 2.4 mm Ti wire, for instance, was evaluated by extending the filler wire as shown in Fig. 11a. It was only 0.3 mm past the arc centre as it was largely limited in the longitudinal direction. The arc energy absorbed in the longitudinal direction was much less than that of the 1.2 mm Ti wire which was 1.2 mm past the arc centre (Fig. 11b). Therefore, the highest DR with the 2.4 mm Ti wire was only 25 % instead of a theoretical value of 84 % [10] higher than that with the 1.2 mm Ti wire. However, the highest DR with the 2.4 mm Ti wire can be further higher if d_{ws} is increased to a suitable value to modify wire melting and metal transfer [10,12].

The highest DR with the dual Ti wire should be similar to that with the 2.4 mm Ti wire because they have the same total width of 2.4 mm laterally. However, since the thickness of the dual Ti wire was half that of the 2.4 mm Ti wire, the furthest wire feeding position of the dual Ti wire should be larger than that of the 2.4 mm Ti wire. It still achieved 0.6 mm past the arc centre although there was a restriction due to the collision of the two wires (Fig. 11c). The highest DR with the dual Ti wire was 34.8 % larger than that with the 1.2 mm Ti wire, which significantly exceeded that with the 2.4 mm Ti wire. An even higher DR should be achieved by using parallel dual Ti wire with no restriction of the wires' collision during the wire feeding process. Additionally, when the flat MS wire was used, it fully penetrated easily at the centre but was not melted so easily at the sides (Fig. 11e) due to a Gaussian-like arc. Still, more areas of the flat MS wire in both the lateral and longitudinal directions were irradiated by the arc compared to that of the 1.2 mm MS wire (Fig. 11d), resulting in a 78 % higher DR. More wire might be melted when the wire geometry is shaped closer to a Gaussian-like arc distribution.

Although the flat MS wire configuration can provide the highest DR, the deposited bead exhibited large ripples and was not straight (Fig. 5e),
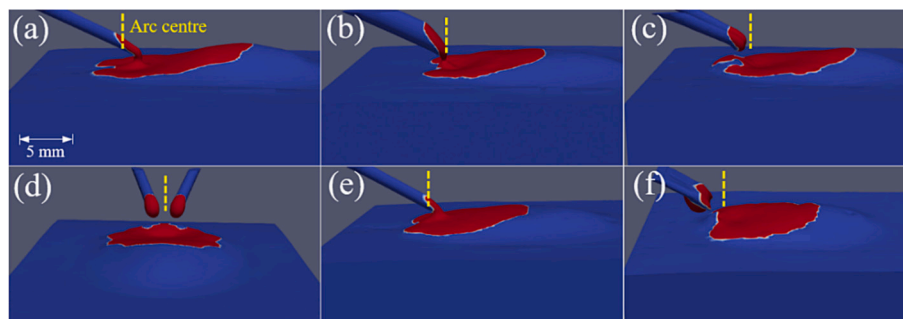

Fig. 7. Simulated wire melting behaviours for the five wire configurations: (a) 1.2 mm Ti wire; (b) 2.4 mm Ti wire; (c) dual Ti wire (longitudinal view); (d) dual Ti wire (lateral view); (e) 1.2 mm MS wire; (f) flat MS wire.
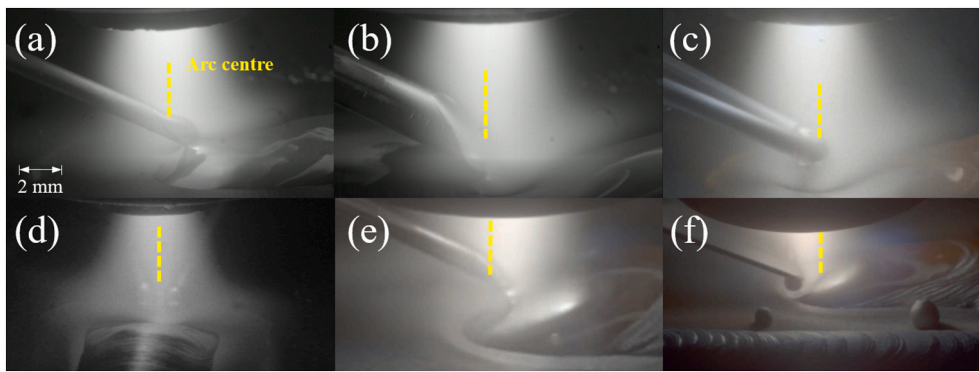
Fig. 8. Process images of wire melting behaviours for the five wire configurations: (a) 1.2 mm Ti wire; (b) 2.4 mm Ti wire; (c) dual Ti wire (longitudinal view); (d) dual Ti wire (lateral view); (e) 1.2 mm MS wire; (f) flat MS wire.
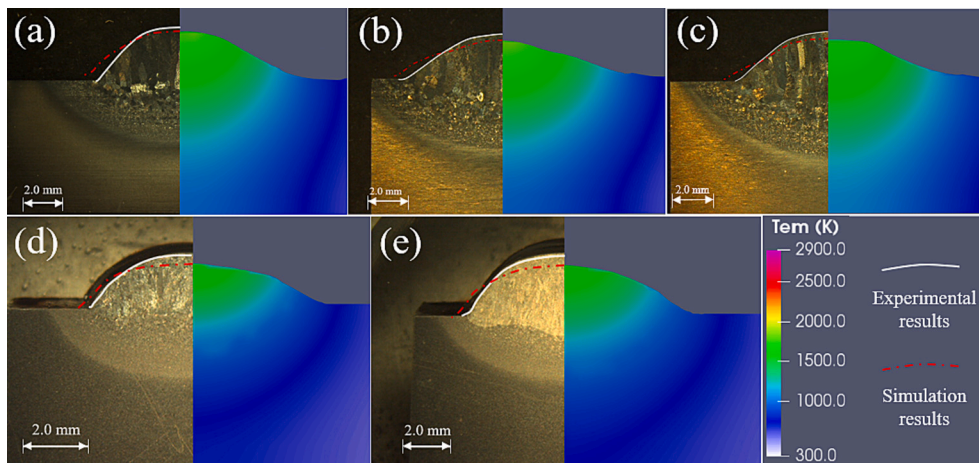

Fig. 9. Cross-sections of the simulated and experimentally measured beads for the five wire configurations: (a) 1.2 mm Ti wire; (b) 2.4 mm Ti wire; (c) dual Ti wire; (d) 1.2 mm MS wire; (e) flat MS wire.

Table 7
Comparisons of the bead dimensions between simulations and experiments.

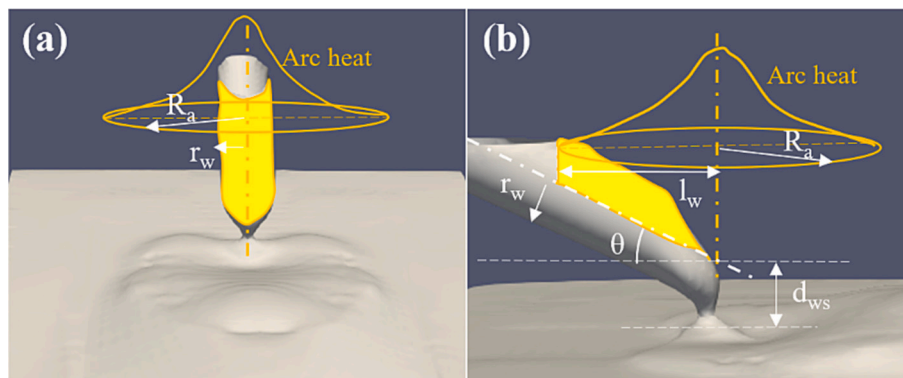| Wire configuration	Bead width (mm)			Bead height (mm)			Penetration depth (mm)		
	Exp.	Sim.	Error	Exp.	Sim.	Error	Exp.	Sim.	Error
1.2 mm Ti wire	8.33	9	8 %	2.74	2.71	1 %	1.54	1.8	16.9 %
2.4 mm Ti wire	9.41	10	6.3 %	2.22	2.1	5.4 %	1.62	1.6	1.2 %
Dual Ti wire	9.38	9.6	2.3 %	2.62	2.4	8.4 %	1.8	2.0	11.1 %
1.2 mm MS wire	8.6	9.6	11.6 %	2.03	1.76	13.3 %	0.73	0.6	17.8 %
Flat MS wire	8.46	9.5	12.3 %	2.3	2	13 %	0.92	1.0	8.7 %

Fig. 10. Arc energy absorption on the filler wire in the lateral (a) and longitudinal (b) directions.
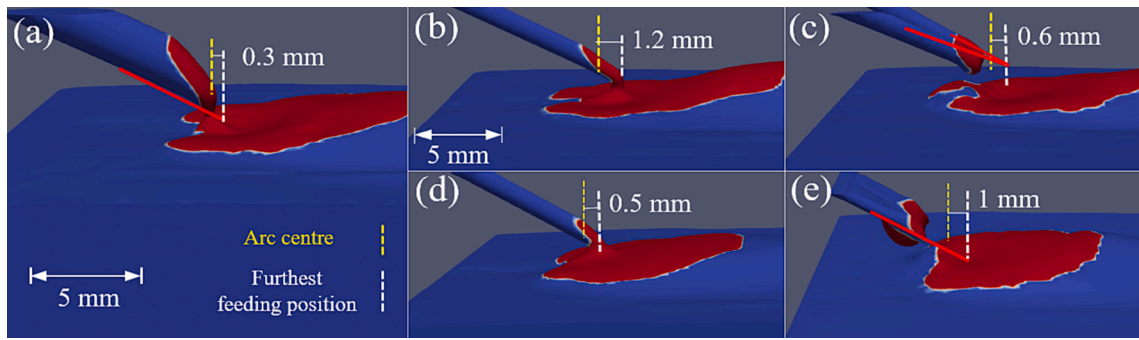
Fig. 11. The wire melting and potential furthest wire feeding positions at the longitudinal direction for the five wire configurations: (a) 1.2 mm Ti wire; (b) 2.4 mm Ti wire; (c) dual Ti wire; (d) 1.2 mm MS wire; (e) flat MS wire.
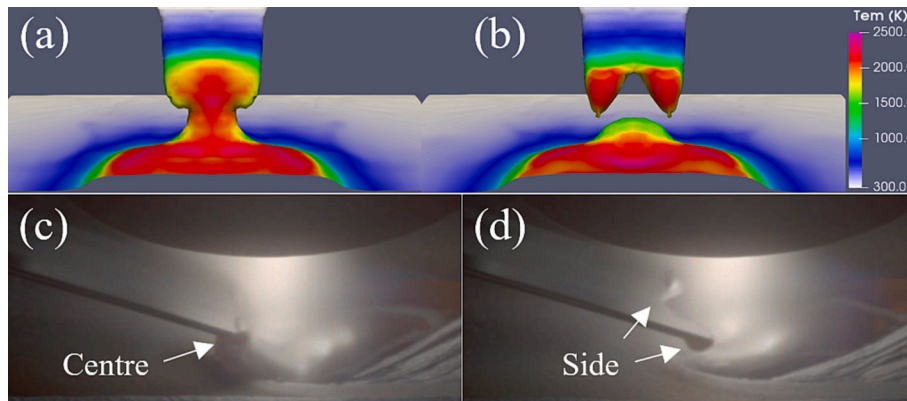

Fig. 12. The melted flat MS wire transferred from different positions of the wire in the simulation results (a and b) and experimental images (c and d): (a) centre; (b) side; (c) centre; (d) side.

which suggested unstable metal transfer. To investigate the metal transfer behaviour, simulations and process images were analysed (Fig. 12), which showed that the melted wire could be transferred to the melt pool from either the wire centre or the wire sides. However, the high-density energy and pressure, distributed in a Gaussian pattern, were concentrated in a small region (approximately 2 mm radius in this study [12,35]). This caused the central part of the 5 mm wide flat MS wire to be melted and blown down by the high-density arc pressure, resulting in a central wire transfer (Fig. 12a and c). Meanwhile, the wire sides were gradually melted and transferred to the melt pool, resulting in a side wire transfer (Fig. 12b and d). These metal transfers alternated during the deposition process, leading to unstable metal transfer and a non-straight bead with large ripples. To obtain a more stable metal transfer and smoother bead, the wire along the lateral direction is better to be melted and transferred to the melt pool at the same time.

Therefore, the width of the flat wire should be decreased to 4 mm or even less, or the wire geometry should be adjusted to a shape closer to a Gaussian-like distribution.

In conclusion, the highest DR in the plasma-DED process is affected by the arc's absorption on the wire, including the absorption area and arc energy distribution. Both dual wire and flat wire have the potential to achieve significantly higher DR compared with the conventional 1.2 mm single wire. The wire along the lateral direction melted and transferred to the melt pool at the same time might achieve the highest DR and stable metal transfer. Consequently, the filler wire geometry designed as a Gaussian-like arc distribution or a close one might get the highest DR and stable metal transfer.

To further demonstrate the above findings, the wire melting behaviours with two additional MS wire configurations with the same WFS used were simulated to compare with that of the flat MS wire, as shown
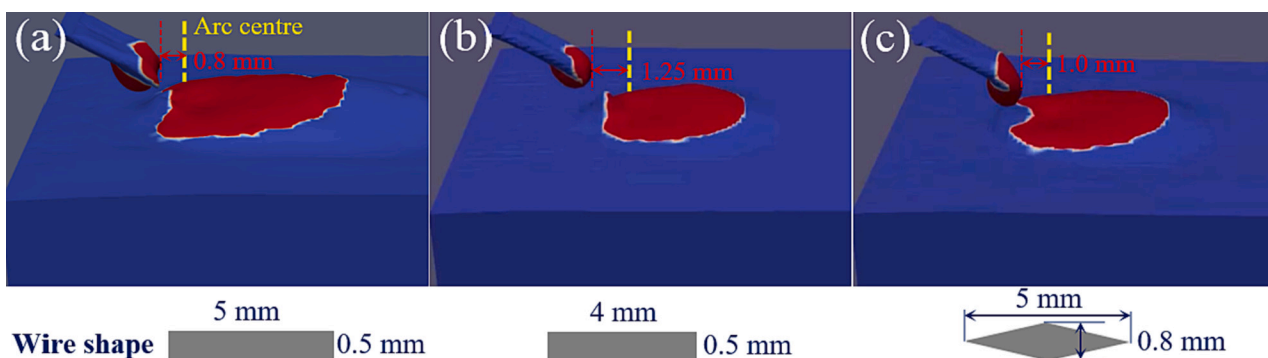

Fig. 13. The wire melting of the flat MS wire (a) and two additional MS wires: (b) a narrower flat MS wire with a width of 4.0 mm; (c) a rhombus MS wire with a width of 5.0 mm and a thickness of 0.8 mm.

in Fig. 13. A narrower flat wire with a width of 4 mm (Fig. 13b) was utilized to assess metal transfer stability compared to that of the flat MS wire (Fig. 13a). Additionally, a rhombus wire, which has the same cross-section area with a width of 5 mm and a thickness of 0.8 mm and a shape closer to a Gaussian distribution than the flat MS wire, (Fig. 13c), was used to evaluate the highest DR and transfer stability compared to that of the flat MS wire.

As illustrated in Fig. 13, the metal transfer with the narrower flat wire was more stable with almost no side wire transfer during the wire feeding process, compared to that of the flat MS wire. Furthermore, when the rhombus wire was used (Fig. 13c), the metal transfer was even more stable than the previous two flat wires (Fig. 13a and b). Additionally, the rhombus wire was fully melted in the centre and sides easily, and the metal transfer position was 1.0 mm past the arc centre, which indicates the wire melting was also better than that of the flat MS wire with a metal transfer position of 0.8 mm past the arc centre. Consequently, the highest DR with the rhombus wire was also higher than that with the flat MS wire. These results further demonstrate that the filler wire configuration significantly affects the DR and metal transfer stability. As the melting and transfer of the filler wire within the limited wire feeding time are also dependent on the wire materials' properties, further optimisation of wire geometry is needed and will be performed in future work.

3.3.2. Melt pool dynamics and bead formation

In arc welding or arc-DED processes, the melt pool behaviour especially the fluid flows, are an essential factor contributing to the bead formation [20–22,36]. To understand the effect of filler wire on the bead formation in the plasma-DED process, the melt pool behaviours using the five wire configurations were investigated numerically. A constant DR was maintained for identical wire materials: as mentioned above, the DR for all Ti64 wires is 1.224 kg/h, while 1.18 kg/h for both MS wires. Fig. 14 shows longitudinal central slices of the fluid flow in the melt pool during a quasi-steady state (after 3.0 s) using the 2.4 mm Ti wire. The transient dynamics of the melt pool formation before reaching the quasi-steady state were discussed in our previous work [12]. When the melted wire touched the melt pool or substrate, it impacted the surface and accelerated the backward and lateral flows (Fig. 14a). After a while, the backward flows near the back solid edge in the rear melt pool increased from 0.1 m/s to 0.15 m/s (Fig. 14b). As deposition progressed, the impact of the melted wire on the melt pool decreased, causing the backward flows near the back solid edge to decrease to 0.08 m/s (Fig. 14c). When the melted wire impacted the melt pool again, the backward flows were accelerated to 0.12 m/s (Fig. 14d). These dynamic behaviours occurred periodically and contributed to the metal transport from the melted wire to the deposit. The maximum flow velocities of the

backward and lateral flows near the back and side solid edges were closely related to the bead height and width. Therefore, the effects of wire configuration on the backward and lateral flows were further studied in the following sections.

Fig. 15 shows the melt pool behaviours using the 1.2 mm Ti wire, the 2.4 mm Ti wire, and the dual Ti wire in a quasi-steady state. Four slices (slices 1–4) were taken to provide a comprehensive analysis of the melt pool behaviours, including three lateral slices positioned 1 mm ahead of the metal transfer, at the metal transfer, 2 mm behind the arc centre, and a longitudinal central slice. When using the 1.2 mm Ti wire (Fig. 15a), the metal transfer position passed the arc centre and created a low-temperature melt pool at the centre before the metal transfer (Fig. 15a1) due to the arc shading effect caused by the filler wire [12]. The metal transfer then impacted the melt pool surface, resulting in accelerated fluid flow in the back and side directions (Fig. 15a and a2). However, an inward Marangoni force caused by the lower temperature in the central melt pool (2830 K) compared to the temperature beside it (2920 K), slowed down the lateral flows, making them mild (0.18 m/s) near the side solid edge (Fig. 15a3). In contrast, the backward flows near the back solid edge were very intensive (0.35 m/s) (Fig. 15a4).

Using the 2.4 mm Ti wire (Fig. 15b) caused the melted wire to be located at the arc centre while transferring to the melt pool, but the substrate was not fully melted when the metal transfer occurred due to the strong arc shading effect produced by the 2.4 mm Ti wire (Fig. 15b1 and b2). This effect decreased the impact of the melted wire on backward flows, which reached a maximum of only 0.15 m/s near the solid back edge (Fig. 15b4). However, the melted wire was still able to transfer to the side melt pools, accelerating the lateral flows. In addition, the strong sideward Marangoni force produced by the high temperature of 2980 K in the central metal pool resulted in intensive lateral flows, reaching a velocity of 0.35 m/s near the side solid edge.

Using the dual Ti wire (Fig. 15c) positioned the melted wire transfer closer to the arc centre, but the arc shading effect was still observed (Fig. 15c1), dividing the melt pool into three smaller pools due to the unmelted parts underneath the dual Ti wire (Fig. 15c2). The melted wire impacted these three pools, accelerating backwards and lateral flows. The backward flows near the back solid edge reached 0.3 m/s (Fig. 15c4), and the lateral flows were intensified due to the sideward Marangoni force produced by the high temperature of 2930 K in the central melt pool (Fig. 15c3), with the lateral flows reaching 0.25 m/s near the side solid edge. These findings suggest that the filler wire configuration plays a significant role in bead formation by influencing the thermal transfer and fluid flows in the melt pool. The maximum velocity of the lateral and backward flows near the side and back solid edges correspond to the variation in bead width and height observed with the 1.2 mm Ti wire, the 2.4 mm Ti wire, and the dual Ti wire.
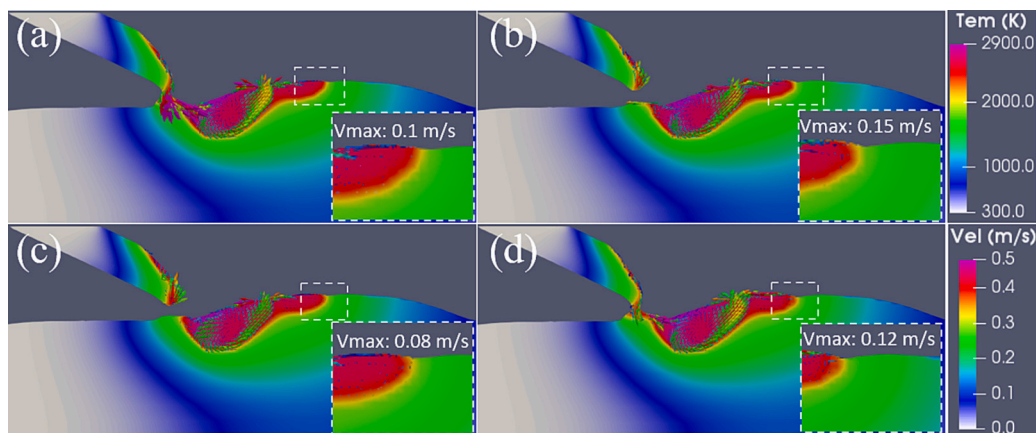

Fig. 14. Longitudinal central slices of fluid flow in the melt pool during a quasi-steady state (after 3.0 s) for the 2.4 mm Ti wire: (a) 3.1906 s; (b) 3.2146 s; (c) 3.2386 s; (d) 3.2866 s.
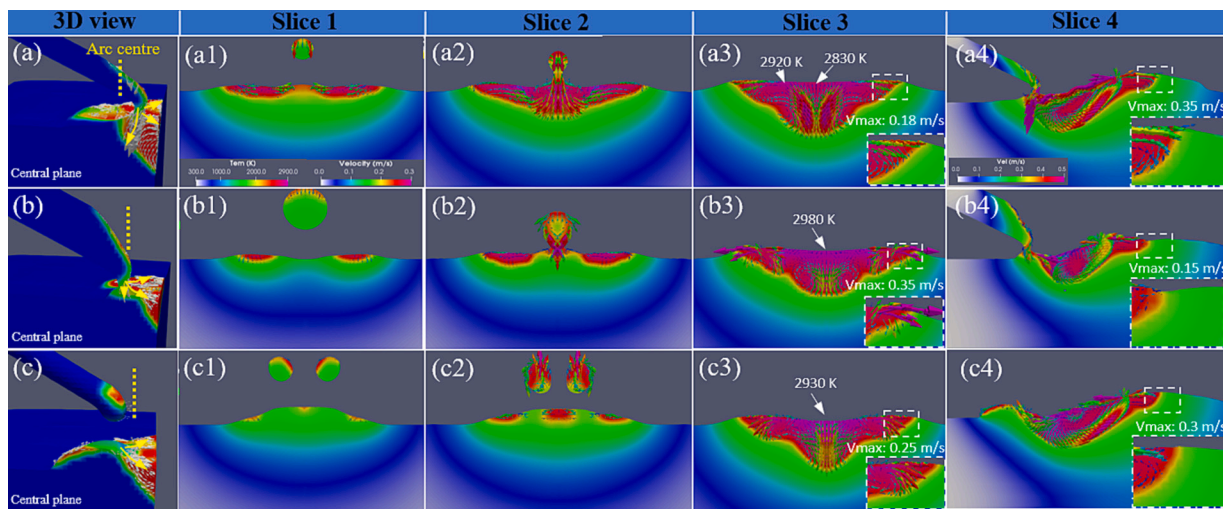
Fig. 15. Metal transfer, temperature distribution and fluid flow for the three Ti64 wire configurations.
(slices 1–4 are three lateral slices positioned 1 mm ahead of the transfer position, at the transfer position, and at 2 mm behind the arc centre and a longitudinal central slice): (a–a4) 1.2 mm Ti wire; (b–b4) 2.4 mm Ti wire; (c–c4) dual Ti wire.
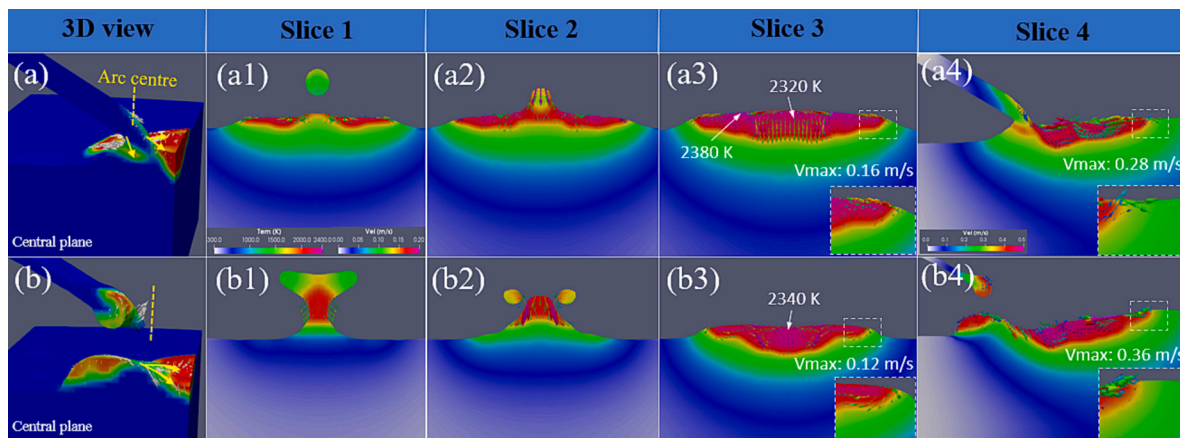

Fig. 16. Metal transfer, temperature distribution and fluid flows during the deposition of mild steel for the two MS wire configurations (slices 1–4 are three lateral slices positioned 1 mm ahead of the transfer position, at the transfer position, and at 2 mm behind the arc centre and a longitudinal central slice): (a–a4) 1.2 mm MS wire; (b–b4) flat MS wire.

Fig. 16 shows the melt pool behaviours using the 1.2 mm MS wire and the flat MS wire in a quasi-steady state. Four slices (slices 1–4) were taken to provide a comprehensive analysis of the melt pool behaviours, including three lateral slices positioned 1 mm ahead of the metal transfer, at the metal transfer, 2 mm behind the arc centre, and a longitudinal central slice. With the 1.2 mm MS wire, the metal transfer position passed the arc centre (Fig. 16a), forming a melt pool with a low temperature at the centre (Fig. 16a1). During the metal transfer, the melted wire flowed down, impacting the melt pool surface, and accelerating the backward and lateral flows (Fig. 16a and a2). The backward flows near the solid back edge could reach up to 0.28 m/s (Fig. 16a4), while the lateral flows near the solid back edge were slower due to an inward Marangoni force caused by the lower temperature at the central melt pool (2320 K) than besides (2380 K) (Fig. 16a3). This resulted in lateral flows near the solid side edge reaching only 0.16 m/s.

In contrast, with the flat MS wire, the melted wire was away from the arc centre (Fig. 16b), resulting in the substrate underneath the wire remaining unmelted and no melt pool being formed due to the strong arc shading effect caused by the wide flat MS wire (Fig. 16b1 and b2). This led to weak preheating in front of the melt pool, which reduced the lateral flows significantly. However, the backward flows in the melt pool at the solid back edge could reach up to 0.38 m/s (Fig. 16b4), which was

larger than that using the 1.2 mm MS wire. Although the lateral Marangoni flows were intensive due to a high temperature (2340 K) in the central metal pool, the lateral flows near the side solid edge were very mild at 0.12 m/s (Fig. 16b3), which was smaller than that using the 1.2 mm MS wire. Thus, the maximum velocity of the lateral and backward flows near the side and back solid edges correspond to the variation in bead width and height observed with the 1.2 mm MS wire and flat MS wire. Those further demonstrate that the filler wire configuration significantly influences the bead dimensions by affecting the thermal transfer and fluid flows in the melt pool in the plasma-DED process.

4. Conclusions

The key findings of this study are as follows:

(1) The filler wire configuration, including the wire width, thickness and geometry, plays a significant role in the wire melting and thus the highest DR. In the current study, the dual wire and flat wire can obtain a higher DR than the other wire configurations.
(2) The wide flat wire is prone to regular alternation of the transfer position from the wire centre to edge, leading to unstable metal transfer and non-straight beads with large ripples. A rhombus

wire with a geometry closer to a Gaussian-like distribution than the flat wire can achieve a higher DR and better metal transfer.

(3) The filler wire configuration can alter the metal transfer behaviours and arc shading effect, which significantly affects the melt pool behaviours, such as temperature distribution and flow velocity, ultimately influencing the final bead formation. This reveals the fundamental physics of the effect of filler wire configuration on the bead formation.

Supplementary data to this article can be found online at https://doi.org/10.1016/j.jmapro.2023.10.020.

Declaration of competing interest

The authors declare that they have no known competing financial interests or personal relationships that could have appeared to influence the work reported in this paper.

Data availability

Data underlying this study including Videos 1 and 2 (Simulated wire melting and its evolution with the dual Ti wire in longitudinal view and lateral view) and Video 3 and 4 (Process images of wire melting and its evolution with the dual Ti wire in longitudinal view and lateral review) can be accessed through the Cranfield University repository at https://doi.org/10.17862/cranfield.rd.24316675.

Acknowledgements

References

[1] DebRoy T, Wei HL, Zuback JS, Mukherjee T, Elmer JW, Milewski JO, et al. Additive manufacturing of metallic components process, structure and properties. Prog Mater Sci 2018;92:112–224.

[2] Gu D, Shi X, Poprawe R, Bourell DL, Setchi R, Zhu J. Material-structure-performance integrated laser-metal additive manufacturing. Sci. 2021;372:1487.

[3] King WE, Anderson AT, Ferencz RM, Hodge NE, Kamath C, Khairallah SA, et al. Laser powder bed fusion additive manufacturing of metals; physics, computational, and materials challenges. Appl Phys Rev 2015;2:041304.

[4] Herzog D, Seyda V, Wycisk E, Emmelmann C. Additive manufacturing of metals. Acta Mater 2016;117:371–92.

[5] Williams S, Martina F, Addison AC, Ding J, Pardal G, Colegrove P. Wire+ arc additive manufacturing. Mater Sci Technol 2016;32:641–7.

[6] Zhang Y, Chen Y, Li P, Male AT. Weld deposition-based rapid prototyping: a preliminary study. J Mater Process Technol 2003;135:347–57.

[7] Busachi A, Erkoyuncu J, Colegrove P, Martina F, Ding J. Designing a WAAM based manufacturing system for defence applications. Proc Cirp 2015;37:48–53.

[8] Quegueineur A, Rückert G, Cortial F, Hascoët JY. Evaluation of wire arc additive manufacturing for large-sized components in naval applications. Weld World 2018; 62:259–66.

[9] Ding J, Colegrove P, Mehnen J, Ganguly S, Sequeira Almeida PM, Wang F, et al. Thermo-mechanical analysis of wire and arc additive layer manufacturing process on large multilayer parts. Comput Mater Sci 2011;50:3315–22.

[10] Wang C, Suder W, Ding J, Williams S. The effect of wire size on high deposition rate wire and plasma arc additive manufacture of Ti-6Al-4V. J Mater Process Technol 2021;288:116842.

[11] Lin J, Lv Y, Liu Y, Xu B, Sun Z, Li Z, et al. Microstructural evolution and mechanical properties of Ti6Al4V wall deposited by pulsed plasma arc additive manufacturing. Mater Des 2016;102:30–40.

[12] Chen X, Wang C, Ding J, Bridgeman P, Williams S. A three-dimensional wire-feeding model for heat and metal transfer, fluid flow, and bead shape in wire plasma arc additive manufacturing. J Manuf Process 2022;83:300–12.

[13] Silwal B, Santangelo M. Effect of vibration and hot-wire gas tungsten arc (GTA) on the geometric shape. J Mater Process Technol 2018;251:138–45.

[14] Murphy AB, Tanaka M, Tashiro S, Sato T, Lowke JJ. A computational investigation of the effectiveness of different shielding gas mixtures for arc welding. J Phys D Appl Phys 2009;42:115205.

[15] Schnick M, Füssel U, Spille-Kohoff A. Numerical investigations of the influence of design parameters, gas composition and electric current in plasma arc welding (PAW). Weld World 2010;54:R87–94.

[16] Feng Y, Zhan B, He J, Wang K. The double-wire feed and plasma arc additive manufacturing process for deposition in Cr-Ni stainless steel. J Mater Process Technol 2018;259:206–15.

[17] Xu T, Liu J, Lu T, Jing C, Wang J, Ma S, et al. Fabrication strategy and macroscopic defect control of large-size component based on double-wire arc additive manufacturing. Int J Adv Manuf Technol 2023;125:2609–25.

[18] Zhao Y, Chung H. Numerical simulation of droplet transfer behavior in variable polarity gas metal arc welding. Int J Heat Mass Trans 2017;111:1129–41.

[19] Hu J, Tsai HL. Heat and mass transfer in gas metal arc welding, part II: the metal. Int J Heat Mass Transf 2007;50:808–20.

[20] Huang J, Li Z, Yu S, Yu X, Fan D. Real-time observation and numerical simulation of the molten pool flow and mass transfer behavior during wire arc additive manufacturing. Weld World 2022;66:481–94.

[21] Zhao W, Wei Y, Long J, Chen J, Liu R, Ou W. Modeling and simulation of heat transfer, fluid flow and geometry morphology in GMAW-based wire arc additive manufacturing. Weld World 2021;65:1571–90.

[22] Ou W, Mukherjee T, Knapp GL, Wei Y, DebRoy T. Fusion zone geometries, cooling rates and solidification parameters during wire arc additive manufacturing. Int J Heat Mass Transf 2018;127:1084–94.

[23] Cadiou S, Courtois M, Carin M, Berckmans W, LeMasson P. Heat transfer, fluid flow and electromagnetic model of droplets generation and molten pool behavior for wire arc additive manufacturing. Int J Heat Mass Transf 2020;148:119102.

[24] Fan S, Yang F, Zhu X, Diao Z, Chen L, Rong M. Numerical analysis on the effect of process parameters on deposition geometry in wire arc additive manufacturing. Plasma Sci Technol 2022;24:044001.

[25] Dou Z, Lyu F, Wang L, Gao C, Zhan X. Relationship between droplet transfer and forming quality in wire arc additive manufacturing of 2319 aluminum alloy. Int J Adv Manuf Technol 2023:1–14.

[26] Ríos S, Colegrove P, Williams S. Metal transfer modes in plasma wire + arc additive manufacture. J Mater Process Technol 2019;264:45–54.

[27] Jia C, Liu W, Chen M, Guo M, Wu S, Wu C. Investigation on arc plasma, droplet, and molten pool behaviours in compulsively constricted WAAM. Add Manuf 2020; 34:101235.

[28] Chen G, Williams S, Ding J, Wang C, Suder W. Multi-energy source (MES) configuration for bead shape control in wire-based directed energy deposition (w-DED). J Mater Process Technol 2022;304:117549.

[29] Hu R, Chen X, Yang G, Gong S, Pang S. Metal transfer in wire feeding-based electron beam 3D printing: modes, dynamics, and transition criterion. Int J Heat Mass Transf 2018;126:877–87.

[30] Hirt C, Nichols B. Volume of fluid (VOF) method for the dynamics of free boundaries. J Comput Phys 1981;39:201–25.

[31] Voller V, Brent A, Prakash C. The modelling of heat, mass and solute transport in solidification systems. Int J Heat Mass Transf 1989;32:1719–31.

[32] Chen X, Mu Z, Hu R, Liang L, Murphy AB, Pang S. A unified model for coupling mesoscopic dynamics of keyhole, metal vapor, arc plasma, and weld pool in laser-arc hybrid welding. J Manuf Process 2019;41:119–34.

[33] Bai X, Colegrove P, Ding J, Zhou X, Diao C, Bridgeman P, et al. Numerical analysis of heat transfer and fluid flow in multilayer deposition of PAW-based wire and arc additive manufacturing. Int J Heat Mass Trans 2018;124:504–16.

[34] Cadiou S, Courtois M, Carin M, Berckmans W. 3D heat transfer, fluid flow and electromagnetic model for cold metal transfer wire arc additive manufacturing (Cmt-Waam). Add Manuf 2020;36:101541.

[35] Chen G, Williams S, Ding J, Wang Y, Suder W. Split anode calorimetry for plasma arc energy density measurement with laser calibration. J Manuf Process 2022;78: 71–81.

[36] Aucott L, Dong H, Mirihanage W, Atwood R, Kidess A, Gao S, et al. Revealing internal flow behaviour in arc welding and additive manufacturing of metals. Nat Commun 2018;9:5414.

Thermal fluid dynamics of the effect of filler wire on deposition rate and bead formation intending plasma arc-based DED

Chen, Xin